PAPER

Check for updates

Fabrication and evaluation of PLA/CPP/GO composite scaffolds: the role of graphene oxide content in regulating properties

Shuqiong Liu, [iD] *[a] Changkun Zhang,[a] Junxia Li,[b] Jiaojiao Zhang,[a] Yan Wang,[a] Jianbo Hua[a] and Yuying Zheng [iD] *[c]

The development of bone tissue engineering scaffolds that combine biomimetic architecture with osteoinductive properties remains a challenge. In this study, a series of poly(lactic acid)/calcium polyphosphate/graphene oxide (PLA/CPP/GO) composite scaffolds with varying GO contents were fabricated *via* phase separation. The influence of GO concentration on the scaffold properties was systematically investigated. Results indicated that the incorporation of GO markedly enhanced the microstructure, hydrophilicity, and bioactivity of the scaffolds. Specifically, at GO loadings of 0.5–1.5 wt%, the scaffolds developed a refined fibrous architecture with highly interconnected pores (porosity > 90%), and demonstrated optimal mechanical strength (compressive strength ~2.34 MPa) and improved wettability. More significantly, GO effectively augmented the biomineralization capacity and osteogenic potential of the scaffolds. *In vitro* biomineralization assays revealed that GO facilitated the deposition of carbonate hydroxyapatite. Cell culture studies further showed that scaffolds with 0.5 wt% GO significantly enhanced alkaline phosphatase (ALP) activity in MC3T3-E1 cells, indicating promoted osteogenic differentiation. This study demonstrates that an appropriate amount of GO can endow PLA/CPP-based scaffolds with favorable mechanical properties, high porosity, excellent bioactivity, and osteoinductivity, making them promising candidates for bone tissue engineering applications.

1. Introduction

Bone defect repair represents a significant challenge in clinical orthopedics, with approximately 2.2 million bone grafting procedures performed globally each year due to trauma, tumors, or congenital disorders.[1] In response, bone tissue engineering has emerged as a promising alternative, where biodegradable polymer/inorganic composite scaffolds can mimic the structural and compositional complexity of the natural bone extracellular matrix (ECM).[2] An ideal bone scaffold should meet the following requirements: (1) a three-dimensional (3D) interconnected porous structure to support cell infiltration, nutrient transport, and vascularization; (2) suitable mechanical strength to provide mechanical support during bone remodeling; (3) controllable biodegradation synchronized with the rate of new bone formation; and (4) intrinsic bioactivity to stimulate osteogenic differentiation and

mineralization.[3,4] In particular, the ability to induce hydroxyapatite deposition—the primary inorganic component of natural bone—on the scaffold surface is a key indicator of its bioactivity and osteoconductive potential.

Polylactic acid (PLA), an FDA-approved biodegradable polymer, is widely used in bone repair owing to its excellent biocompatibility, ease of processing, and tunable degradation rate.[5] However, its inherent hydrophobicity, release of acidic degradation products (which may cause aseptic inflammation), and lack of osteoinductive properties have restricted its broader clinical use.[6] Calcium polyphosphate (CPP), an inorganic polymer with the formula $[Ca(PO_3)_2]_n$ and a Ca:P ratio of 0.5, exhibits a linear polyphosphate backbone and a high zeta potential (-34 mV).[7] Its chemical similarity to natural bone mineral enables excellent osteoconductivity, biodegradability, bioactivity, and pH-buffering capability.[8] Nevertheless, CPP-based scaffolds suffer from high brittleness, poor formability, and a lack of antibacterial activity, limiting their standalone application.[9]

To address the limitations of individual components, organic–inorganic composites have been developed to combine the flexibility of polymers with the bioactivity of ceramics. For instance, Liu *et al.* demonstrated that silk fibroin/CPP composite hydrogels enhanced alkaline phosphatase (ALP) activity and mineralization of bone marrow mesenchymal stem cells (BMSCs) compared to

[a] Fujian Provincial Key Laboratory of Eco-Industrial Green Technology, College of Ecology and Resources Engineering, Wuyi University, Wuyishan 354300, People's Republic of China. E-mail: liuhsuqiong123456@163.com; Tel: +86-599-5136976

[b] School of Materials Science & Engineering, North Minzu University, Yinchuan, 750021, People's Republic of China

[c] College of Materials Science and Engineering, Fuzhou University, Fuzhou, 350108, People's Republic of China

pure silk fibroin scaffolds.[7] Neufurth et al. fabricated calcium polyphosphate/poly(ε-caprolactone)(CPP/PCL) scaffolds with mechanical properties matching those of cortical and trabecular bone, which supported SaOS-2 cell adhesion and proliferation via integrin-mediated signaling.[10] Despite these advances, simple blending strategies often result in weak interfacial bonding, inadequate mechanical strength, and suboptimal hydrophilicity.[11]

Recently, nanomaterial reinforcement has offered a breakthrough in composite scaffold design. Graphene oxide (GO), a two-dimensional (2D) carbon nanomaterial with a honeycomb lattice, has garnered attention in biomaterials due to its exceptional mechanical properties ($\sim$130 GPa), large specific surface area ($\sim$2600 m^2 g^{-1}),[12,13] and abundant surface functional groups (–COOH, –OH, C–O–C).[14] These features enable GO to: (1) serve as a nanoreinforcement to improve mechanical properties; (2) enhance surface hydrophilicity; and (3) promote osteogenic differentiation by activating signaling pathways such as Wnt/β-catenin and MAPK[15–17], upregulating key markers including RUNX2 and osteocalcin.[16] Ahn et al. demonstrated that incorporating graphene oxide (GO) into mesoporous bioactive glass nanoparticles significantly enhanced the osteogenic differentiation of human dental pulp stem cells via Wnt/β-catenin activation and increased ALP activity.[18] Diez-Pascual et al. reported that the addition of GO notably improved key properties of polypropylene fumarate composites, including hydrophilicity, water absorption, biodegradation rate, and thermal stability, in a concentration-dependent manner.[19] Liang et al. found that the addition of GO into nHAC/PLGA(nano-hydroxyapatite/collagen/poly(lactic-co-glycolic acid) scaffolds improved both mechanical strength and hydrophilicity, with the 1.5 wt% GO scaffold showing the highest promotion of osteoblast adhesion and proliferation.[20] However, several fundamental questions remain, including the role of GO content in directing micro-nano architecture, its concentration-dependent cytocompatibility, and the mechanism by which GO regulates biomineralization.

The thermally induced phase separation (TIPS) method is a widely adopted technique for fabricating porous scaffolds, owing to its operational simplicity, controllable pore structure, and ease of incorporating functional components.[21,22] In this work, we designed and prepared a series of PLA/CPP/GO ternary composite scaffolds via TIPS and systematically investigated the effect of GO content (0–2.0 wt%) on their microstructure, mechanical properties, hydrophilicity, porosity, and in vitro bioactivity. A suite of characterization techniques—including SEM, FTIR, XRD, contact angle measurement, mechanical testing, and porosity analysis—was employed to evaluate the scaffolds' physicochemical properties. In vitro biomineralization in simulated body fluid (SBF) and cell culture studies using MC3T3-E1 pre-osteoblasts were conducted to assess their biological performance. This study aims to develop a multifunctional bone tissue scaffold with an optimal combination of structural and functional properties for bone regeneration applications.

2. Materials and methods

2.1 Materials

Crystalline polylactic acid (PLA, 3052D) with an average molecular weight of 250 000 g mol^{-1} was supplied by Nature-Works LLC. The other chemical reagents were used as received: 1,4-dioxane ($C_4H_8O_2$, AR grade) and potassium persulfate ($K_2S_2O_8$, AR grade) from National Medicines Corporation Chemical Reagent Co., Ltd; natural flake graphite (99.99%, 200 mesh) from Rongtai New Material Technology Co., Ltd; concentrated sulfuric acid (H_2SO_4, AR grade) and potassium permanganate ($KMnO_4$, AR grade) from Guangdong Fine Chemical Engineering Technology Research and Development Center; phosphorus pentoxide (P_2O_5, CP grade), hydrogen peroxide (30% H_2O_2, AR grade), barium chloride ($BaCl_2$, AR grade), sodium chloride (NaCl, AR grade), potassium chloride (KCl, AR grade), magnesium chloride hexahydrate ($MgCl_2\cdot6H_2O$, AR grade), calcium chloride dihydrate ($CaCl_2\cdot2H_2O$, AR grade), disodium hydrogen phosphate dodecahydrate ($Na_2HPO_4\cdot12H2O$, AR grade), tris(hydroxymethyl)aminomethane(($CH_2OH)_3CNH_2$, AR grade), anhydrous disodium hydrogen phosphate (Na_2HPO_4, AR grade), potassium dihydrogen phosphate (KH_2PO_4, AR grade), and calcium polyphosphate (CPP, AR grade) from National Medicines Corporation Chemical Reagent Co., Ltd; hydrochloric acid (HCl, AR grade) from Sanming Sanyuan Chemical Reagent Co., Ltd; sodium bicarbonate ($NaHCO_3$, AR grade) and sodium sulfate (Na_2SO_4, AR grade) from Shanghai Zhanyun Chemical Co., Ltd. Deionized water was prepared in our laboratory. Graphene oxide (GO) was synthesized in the laboratory according to a modified Hummers' method. The detailed synthesis procedure and comprehensive characterization (including TEM, Raman, FTIR, XRD, and XPS) of the laboratory-made graphene oxide (GO) have been reported elsewhere.[22]

2.2 Fabrication of PLA/CPP/GO composite scaffolds

PLA/CPP/GO composite scaffolds were fabricated using a thermally induced phase separation technique. The GO content was varied from 0 to 2.0 wt%, a range established in the literature to effectively enhance material properties while mitigating risks of nanosheet agglomeration.[20,22] The CPP content was fixed at 15 wt%, a loading determined to optimally balance bioactive ion release with scaffold structural integrity based on preliminary studies.[23] In a typical procedure, a scaffold with a total mass of 15 g was prepared, wherein PLA accounted for 10 wt% of the total composition. In a typical procedure, predetermined amounts of graphene oxide (GO, 0, 0.5, 1.0, 1.5, or 2.0 wt% relative to PLA) and calcium polyphosphate (CPP, 15 wt% relative to PLA) were placed into a 100 mL beaker. A mixed solvent of 1,4-dioxane and distilled water (volume ratio 9 : 1) was then added. The mixture was subjected to ultrasonication in a bath sonicator (DF-101S, Gongyi Yuhua Instrument Co., Ltd) until a homogeneous dispersion of GO and CPP was achieved. Subsequently, a pre-weighed amount of PLA was introduced into the beaker. The beaker was then immersed in a constant-temperature water bath maintained at 60 °C with continuous

magnetic stirring until the PLA was completely dissolved. A low-temperature incubator was pre-cooled to 0 °C concurrently. Once PLA was completely dissolved, the homogeneous solution was dispensed into 25 mL beakers (approximately 5 mL each). The beakers were transferred to the pre-cooled incubator and aged at 0 °C for 2 h. Subsequently, the samples were rapidly frozen at −40 °C for another 2 h to ensure complete solidification. The frozen samples were lyophilized in a freeze dryer for 7 days until no solvent odor was detected, indicating complete removal. The resulting scaffolds were stored in sealed bags for further use. The scaffolds were labeled as PCG-0, PCG-0.5, PCG-1, PCG-1.5, and PCG-2, corresponding to GO contents of 0, 0.5, 1.0, 1.5, and 2.0 wt% relative to PLA mass, respectively.

2.3 Characterization of PLA/CPP/GO composite scaffolds

The morphological characteristics of the PLA/CPP/GO composite scaffolds were observed using scanning electron microscopy (SEM; Vega 3 sbh, Tescan Co., Ltd) at an accelerating voltage of 5 kV. Before imaging, the samples were cryo-fractured in liquid nitrogen and sputter-coated with a thin gold layer for 150 s using an ion coater (SBC-12, Kyky Technology Co., Ltd). The morphology of the apatite layer formed on the scaffolds after immersion in simulated body fluid (SBF) was also examined under SEM. The crystalline structure of PLA and the phase composition of deposits formed after SBF immersion were analyzed by X-ray diffraction (XRD; D8 Advance, Bruker Ltd) using Cu Kα radiation ($\lambda = 0.15418$ nm). The instrument was operated at 40 kV and 40 mA, with scanning conducted over a 2θ range from 5° to 60° at a speed of 0.5° min^{-1}. Functional groups of the scaffolds and the chemical composition of mineralized deposits were characterized using Fourier transform infrared spectroscopy (FTIR; Nicolet IS5, Thermo Fisher Ltd). Spectra were recorded in transmission mode at a resolution of 4 cm^{-1} with 64 accumulative scans, covering a wavenumber range of 4000–400 cm^{-1}.

2.4 Porosity and hydrophilic properties

The porosity and water absorption capacity of the scaffolds were evaluated according to a previously reported method.[24] The porosity of the scaffolds was determined using the ethanol liquid displacement method, as described in detail in our previous work.[24] Briefly, the dry weight (W_S) of the scaffold was measured. The scaffold was then immersed in ethanol in a pycnometer of known weight (W_1) and subjected to vacuum to remove trapped air and allow ethanol to fully infiltrate the pores. The pycnometer was refilled, and the total weight (W_2) was recorded. After removing the scaffold, the weight of the remaining ethanol and pycnometer (W_3) was measured. The porosity (ε) was calculated using the following equation:

$$\varepsilon(\%) = \frac{W_2 - W_3 - W_S}{W_1 - W_3} \times 100\%$$

The value for each scaffold is the average of seven independent measurements, and data are expressed as mean ± SD.

Hydrophilicity was assessed by measuring the water contact angle and Water absorption. The water contact angle was measured using a contact angle goniometer (PHS-2F, Shanghai Weiye Instrument Co., Ltd) at room temperature (25 °C). A droplet of 4 μL deionized water was automatically deposited onto the scaffold surface. The static contact angle was calculated automatically by the instrument's software using the sessile drop method. For each scaffold group, five independent samples were tested, and on each sample, the measurement was performed at three different locations. The results are expressed as the mean value ± standard deviation.

2.5 Mechanical properties

Uniaxial compression tests were performed using a universal testing machine (AGS-X, Shimadzu Ltd). Cylindrical specimens (diameter: 27 mm; height: 8 mm) were prepared in quintuplicate for each scaffold type. Tests were conducted at a crosshead speed of 1 mm min^{-1} up to 55% strain. The compressive modulus was determined from the slope of the initial linear region (10–20 N load range) of the stress–strain curve. Compressive strength was defined as the maximum stress reached before 50% strain. For each scaffold type, a minimum of five specimens ($n \geq 5$) were tested, and the results are expressed as the mean ± standard deviation.

2.6 Apatite-formation ability

The bioactivity of the scaffolds was evaluated by examining apatite formation upon immersion in 1.5× simulated body fluid (SBF), following a previously work.[22]

2.7 Cell proliferation

MC3T3-E1 cell proliferation on the scaffolds was assessed using a Cell Counting Kit-8 (CCK-8; Invigentech, Cat#: IV08-100). Cells were cultured in Dulbecco's Modified Eagle Medium(DMEM) complete medium at 37 °C under 5% CO$_2$, with medium changed every three days. Scaffolds were cut into pieces (10 mm^2 × 1 mm), sterilized under UV light for 60 min per side, and placed in 48-well plates. Cells were seeded at a density of 6.0 × 10^3 cells per well and incubated for 24, 72, and 120 h. At each time point, the medium was replaced with 500 μL of fresh medium containing 10% CCK-8 reagent. After 2 h of incubation, the supernatant was transferred to a 96-well plate, and absorbance was measured at 450 nm using a microplate reader (TECAN Spark 10 M). All experiments were performed in triplicate, and data are expressed as mean ± SD.

2.8 Alkaline phosphatase (ALP) activity and staining

ALP activity and staining were used to evaluate osteogenic differentiation. MC3T3-E1 cells were seeded in six-well plates at 1.0 × 10^4 cells per well and cultured with different scaffolds. After 7 and 14 days, cells were lysed, and ALP activity was measured using a commercial kit. Absorbance was read at 405 nm. For ALP staining, cells were fixed in 4% paraformaldehyde for 30 min and stained using an ALP detection

kit. Images were acquired under a microscope at 100× magnification.

2.9 Alizarin Red staining (ARS)

Mineralization induced by the PLA/CPP/GO composite scaffolds was evaluated using Alizarin Red S staining. After 14 days of culture, MC3T3-E1 cells were processed as follows. The culture medium was removed, and the cells were gently rinsed with phosphate-buffered saline (PBS). Fixation was performed using 4% paraformaldehyde for 15 minutes at room temperature. After fixation, the solution was aspirated and the cells were washed again with PBS. Alizarin Red S staining solution (0.2%, Beyotime, C0148S) was then applied to completely cover the cell layer, followed by incubation at 37 °C for 30 minutes. After staining, the cells were rinsed with PBS to remove non-specific dye and imaged under an optical microscope at 100× magnification.

2.10 Statistical analysis

All experiments were performed with at least three independent replicates ($n = 3$) with scaffolds from different fabrication batches. Data are presented as mean ± standard deviation. Statistical significance was determined by one-way ANOVA followed by Tukey's post-hoc test using GraphPad Prism 9.5 software. A value of $p < 0.05$ was considered statistically significant.

3. Results and discussion

3.1 Morphology of PLA/CPP/GO composite scaffolds

The morphological characteristics of tissue engineering scaffolds are paramount, as they directly dictate cellular behavior, including adhesion, proliferation, and differentiation. Fig. 1 shows the cross-sectional morphology of PLA/CPP/GO composite scaffolds with varying GO contents. As observed in Fig. 1(a1–a3), the scaffold without GO exhibits a structure formed by the aggregation of spherical crystalline domains, which are themselves composed of micro-to nano-scaled fibrous networks. These scaffolds display a homogeneous pore architecture with well-distributed porosity, characteristic of the phase-separated pure PLA structure.[22,23] The observed aggregation of spherical crystals forming a micro-nano fibrous network in the pure PLA/CPP scaffold (Fig. 1(a1–a3)) is a typical outcome of the liquid–liquid phase separation process.[25] This structure serendipitously mimics the hierarchical architecture of the native bone extracellular matrix (ECM), which comprises collagen fibrils at the nanoscale and larger fibrous bundles at the microscale. This biomimicry is crucial, as it provides a familiar topological environment for cells, enhancing osteoblast attachment and activity.[26] With the incorporation of GO (Fig. 1b and e), the overall scaffold architecture remains largely unchanged and continues to be based on the assembly of spherical crystalline units. However, with increasing GO content, the boundaries between these spheres become less distinct, and the interconnections among them appear enhanced. The blurring of spherical crystal outlines and the tighter interconnections suggest that GO may acts as
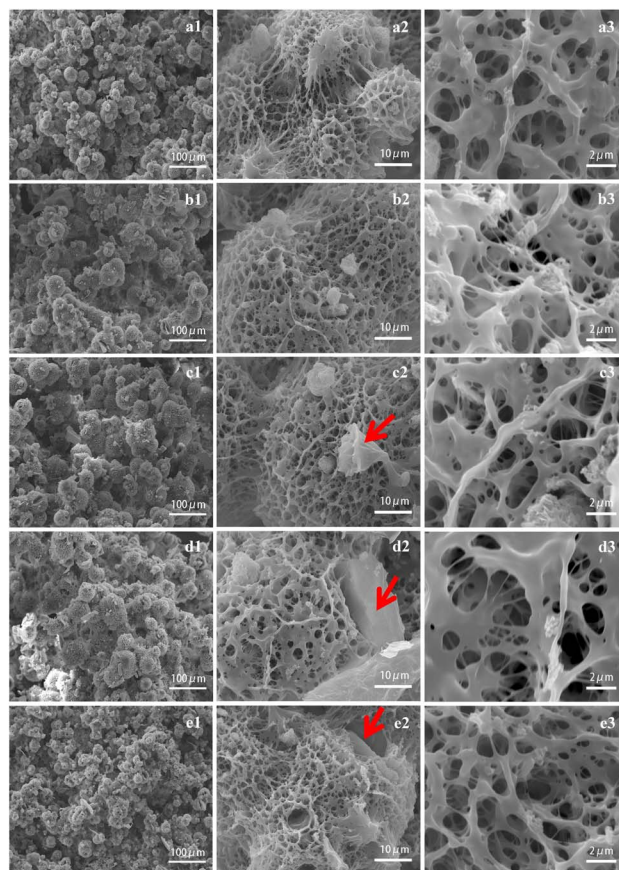

Fig. 1 Shows the evolution of the morphology of the PLA/CPP/GO scaffolds as a function of GO content: (a) PCG-0; (b) PCG-0.5; (c) PCG-1.0; (d) PCG-1.5; (e) PCG-2.0.

a compatibilizer and structural reinforcer within the polymer blend. This can be attributed to the interactions (*e.g.*, hydrogen bonding, π–π interactions) between the oxygen-containing functional groups on GO and the polymer chains, which improve interfacial adhesion and reduce phase separation scale, leading to a more cohesive and integrated structure.[27] This is a critical finding, as poor interfacial compatibility is a common challenge in polymer/ceramic/graphene-based composite scaffolds. Furthermore, the gradual refinement of the internal fibers to the nanoscale with increasing GO content is particularly noteworthy. Previous studies have shown that the addition of GO reduces the fiber diameter of the PCL/GO composite scaffold and increases its water absorption rate.[28] Nanofibrous structures have been extensively reported to promote protein adsorption and provide a larger surface area for cell membrane receptors (*e.g.*, integrins) to engage with, thereby significantly boosting initial cell adhesion compared to smooth or micro-scaled surfaces.[29,30] This effect, combined with the increased pore interconnectivity, creates a highly conducive environment for cell migration, vascularization, and nutrient/waste exchange—factors often limiting the success of large tissue-engineered constructs.[31,32]

It is also evident from Fig. 1 that sheet-like structures, attributed to partially undispersed GO, appear on the surface of

the spherical crystals with higher GO loading. Similar morphological features have been observed in previously fabricated PLA/GO and PLA/GO/ASA scaffolds.[22] The presence of sheet-like GO aggregates, while potentially indicative of a solubility limit, may not be entirely detrimental. As hypothesized, such exposed GO nanosheets have been shown to dramatically improve the hydrophilicity of otherwise hydrophobic polymer scaffolds like PLA.[33] Studies indicate that these sheet-like formations can enhance the water absorption capacity of the scaffold, which is critically important for improving cell adhesion and overall scaffold bioactivity.[33] The hydrophilic nature of GO arises from its abundant hydroxyl and carboxyl groups, which can also facilitate the nucleation of hydroxyapatite during bio-mineralization in simulated body fluid (SBF), a key indicator of bioactivity. Wu *et al.*'s research also indicates that the enhancement of mineralization ability is mainly due to the hydrophilicity and negative charges on the surface of the scaffold, which attract calcium ions[34] However, it is essential to acknowledge a potential trade-off. Excessive GO aggregation could act as stress concentration points, potentially compromising the mechanical integrity of the scaffold under load. Therefore, identifying the optimal GO content that maximizes hydrophilic and biological benefits without negatively impacting mechanical properties will be a key focus of our subsequent investigations. In conclusion, the introduction of GO into the PLA/CPP system successfully engineers a superior micro-nano architecture that is more biomimetic, hydrophilic, and interconnected. These structural enhancements are expected to translate to improved biological performance in terms of cell adhesion, differentiation, and ultimately, bone tissue formation.

3.2 FTIR of PLA/CPP/GO composite scaffolds

Fig. 2 presents the FTIR spectra of PLA/CPP/GO composite scaffolds with varying GO contents. Several characteristic absorption bands can be identified, confirming the chemical constituents and interactions within the composites. Notably, strong peaks are observed at approximately 1753 cm^{-1} and 1083 cm^{-1}, corresponding to the C=O stretching vibration of the ester carbonyl group and the C–O–C stretching vibration, respectively, both indicative of the presence of PLA.[35] The

infrared profile of CPP is characterized by distinctive peaks at 1271 cm^{-1} (P=O stretching), 1090 cm^{-1} (O–P–O stretching), 901 cm^{-1} (asymmetric stretching of P–O–P), 779 cm^{-1} (symmetric stretching of P–O–P), and 541 cm^{-1} (bending mode of $[PO_4]^{3-}$).[7,36,37] In our composite scaffolds, the appearance of absorption bands at 1274 cm^{-1}, 873 cm^{-1}, 600 cm^{-1}, and 560 cm^{-1} aligns well with these reported values, confirming the successful incorporation of CPP into the PLA matrix. With the introduction of GO, the intensities of the ester-related peaks at 1753 cm^{-1} and 1083 cm^{-1} are noticeably enhanced compared to the GO-free scaffold. This observation suggests the presence of graphene oxide and possible molecular interactions between GO and PLA. The enhancement in the characteristic ester peaks can be attributed to the overlapping vibrational modes originating from both PLA and GO, as well as potential newly formed covalent bonds. This proposed molecular-level interaction offers a compelling explanation for the microstructural changes observed in our SEM analysis (Fig. 1). The blurring of spherical crystal boundaries and the tighter interconnection observed by SEM, combined with the shifts in FTIR spectra, suggest improved interfacial compatibility. This indicates that GO may potentially act as a compatibilizer between PLA and CPP, possibly through polar interactions and hydrogen bonding. We posit that GO acts as a multifunctional interfacial agent. The oxygen functional groups on GO can form hydrogen bonds with the ester linkages of PLA, while its large, rigid basal plane can interact with CPP particles through physisorption or polar interactions. This bridging effect reduces the interfacial energy between the organic and inorganic phases, leading to a more cohesive and integrated composite structure, as seen in the refined and continuous micro-nano fibrous network. A recent study by Busra Oktay *et al.* on PLA/hydroxyapatite/GO composites demonstrated a similar role of GO, where enhanced interfacial adhesion, resulted in a more uniform microstructure and significantly improved mechanical properties.[38] The FTIR analysis provides crucial evidence for the successful fabrication of the PLA/CPP/GO ternary composite scaffolds and offers insights into the chemical interactions between the components. These chemical interactions are directly linked to the favorable morphological evolution observed by SEM and lay a strong foundation for the enhanced mechanical and biological properties anticipated in the designed scaffolds.

Fig. 2 FTIR spectra of PLA/CPP/GO composite scaffolds with different GO contents.

3.3 XRD of PLA/CPP/GO composite scaffolds

Fig. 3 displays the XRD diffractograms of PLA/CPP/GO composite scaffolds with varying GO contents. All scaffolds exhibit characteristic diffraction peaks of PLA at approximately 16.5° and 19.5°, corresponding to the (200)/(110) and (203) crystalline planes, respectively.[39] The positions of these peaks remain unchanged regardless of GO or CPP incorporation, indicating that the crystalline structure of PLA is not significantly altered by the addition of these components, which is consistent with previous findings on PLA-based nanocomposites.[22] The characteristic peaks of CPP, notably observed at $2\theta = 26.5°$, 29.8°, 32.5°, 40.0°, 47.2°, and 49.8°, are present across all composite samples from PCG-0 to PCG-2, confirming
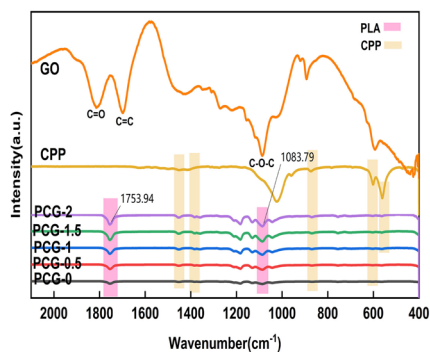
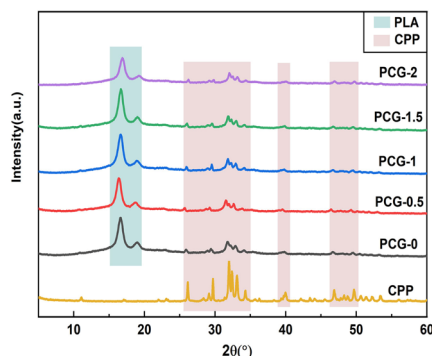**Fig. 3** XRD spectra of PLA/CPP/GO composite scaffolds with different GO contents.

Fig. 4 Contact angles (a) and water absorption (b) of PLA/CPP/GO composite scaffolds with different GO contents.

the successful integration of CPP into the scaffolds. However, the intensity of these peaks is notably reduced, suggesting that CPP is well dispersed and potentially encapsulated by the PLA matrix, limiting its diffraction signal. Notably, no distinct diffraction peak for graphene oxide—typically expected around $2\theta = 10°$—is observed in any of the composites.[40] This absence can be attributed to the low concentration of GO within the detection limit of XRD and possibly to its exfoliation and uniform distribution within the polymer matrix, which disrupts its regular stacking and reduces its crystal signature.[41] This result aligns with earlier reports from our group and others, where GO peaks were only detectable at higher loadings (e.g., ≥3 wt%).[22] Interestingly, the crystallinity of PLA, as inferred from the intensity of its characteristic peaks, shows a non-monotonic trend with increasing GO content. Specifically, the peak intensities decrease initially at lower GO loadings, suggesting that GO may disrupt PLA chain packing and reduce crystallinity. At higher GO concentrations, a rebound in peak intensity indicates that GO may also serve as a nucleating agent, promoting crystallization. This dual effect highlights the role of GO as a modulator of polymeric crystallization behavior, which could further influence the degradation and mechanical properties of the composite scaffolds.

3.4 Water contact angles and water absorption of PLA/CPP/GO composite scaffolds

In bone tissue engineering, the hydrophilic performance of a scaffold is critically important, as it significantly influences protein adsorption, initial cell attachment, and overall biocompatibility. However, the inherent hydrophobicity of polylactic acid (PLA) has limited its broader application in biomedicine.[42] Fig. 4 presents the water contact angle and water absorption of PLA/CPP/GO composite scaffolds with varying GO contents. As shown in the figure, the contact angle exhibits a noticeable decreasing trend with increasing GO incorporation, declining from approximately 123.4° for PCG-0 to 92.0° for PCG-2.0. Conversely, the water absorption capacity significantly improves, rising from 37.26% to 78.89% at the maximum GO loading. These results clearly demonstrate that the incorporation of GO effectively enhances the hydrophilicity of the PLA/CPP-based scaffolds. This improvement can be attributed to the introduction of abundant oxygen-containing functional
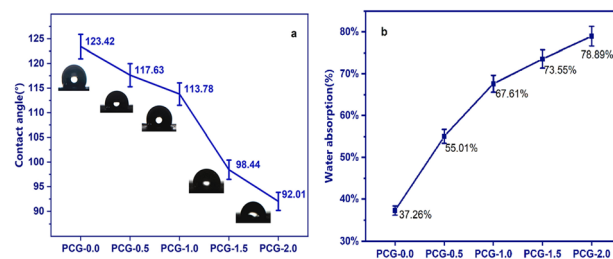
groups (e.g., hydroxyl, epoxy, and carboxyl) on the graphene oxide sheets, which impart strong hydrophilic characteristics to the composite.[43] The gradual reduction in contact angle and concurrent increase in water absorption indicate that GO serves as an effective hydrophilic modifier, overcoming the intrinsic hydrophobic nature of PLA without compromising structural integrity. The enhanced wettability and water uptake behavior are highly desirable for bone tissue engineering applications, as improved hydrophilicity promotes better cell-scaffold interactions and facilitates nutrient diffusion within the porous matrix.[44]

3.5 The porosity of PLA/CPP/GO composite scaffolds

Fig. 5 presents the porosity measurements of PLA/CPP/GO composite scaffolds with varying GO contents. Statistical analysis confirmed that there were no significant differences between groups ($p > 0.05$). However, all scaffolds exhibited consistently high porosity levels exceeding 87%—a value well above the critical threshold of 80% required for effective cell infiltration, vascularization, and nutrient transport in bone tissue engineering.[45] Notably, a consistent trend was observed: the porosity increased with the initial incorporation of GO, reaching a maximum value of 93.26% at 1.0 wt% GO (PCG-1.0), before slightly decreasing to 90.54% and 90.39% at higher loadings (1.5 and 2.0 wt%). Although statistically non-significant, this trend aligns with the microstructural evolution observed by SEM (Fig. 1). It suggests that at optimal concentrations, GO may promote a more interconnected pore network, while at higher loads, agglomeration (as seen in SEM)
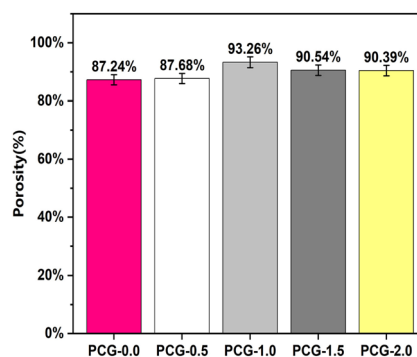

Fig. 5 Porosity of PLA/CPP/GO composite scaffolds with different GO contents. No statistically significant differences were found between the groups ($p > 0.05$, one-way ANOVA). All data are presented as mean ± standard deviation ($n \geq 7$).

might slightly impede pore development. In essence, the incorporation of GO, across all tested concentrations, successfully maintained the scaffold's highly porous nature, which is conducive to bone regeneration.[46,47] The primary outcome is that GO modification does not compromise porosity, while the observed trend provides supportive evidence for GO's role in fine-tuning the microstructure.

3.6 Mechanical properties of PLA/CPP/GO composite scaffolds

The mechanical properties of a scaffold is paramount for its application in bone tissue engineering, as it must withstand physiological loads and provide adequate structural support during the healing process. Fig. 6 illustrates the compressive modulus and compressive strength of PLA/CPP/GO composite scaffolds with varying GO contents. As shown in Fig. 6a, the compressive modulus of the composites initially decreased at a GO content of 0.5% compared to the GO-free scaffold (PCG-0.0). However, a substantial enhancement was observed at 1.0% and 1.5% GO loadings, with the maximum modulus of 2.34 MPa attained at PCG-1.5. A further increase to 2.0% GO led to a notable reduction in modulus, falling even below that of the pure PLA/CPP scaffold. Similarly, the compressive strength (Fig. 6b) generally increased with GO incorporation up to 1.5%, reaching a peak value of 2.34 MPa for PCG-1.5, but declined at 2.0% GO. The non-monotonic variation in mechanical properties can be attributed to the competing effects of GO reinforcement and agglomeration. At moderate concentrations (1.0–1.5%), the well-dispersed GO nanosheets serve as effective reinforcing fillers. Their high specific surface area and strong interfacial interactions with the PLA matrix—*via* hydrogen bonding and possible covalent linkages, as suggested by FTIR—facilitate efficient stress transfer, thereby enhancing both modulus and strength.[48] Furthermore, the refined micromorphology observed *via* SEM, characterized by finer fibers and improved interfacial connectivity, contributes to this reinforcement mechanism. Conversely, the deterioration in performance at high GO content (2.0%) is likely due to nanosheet agglomeration, acting as stress concentrators and defect sites within the matrix. This is consistent with the SEM observations of sheet-like aggregates and the XRD results indicating a reduction in PLA crystallinity—both of which negatively impact mechanical properties. Notably, the compressive strength of scaffolds containing 0.5–1.5% GO all exceeded 2.1 MPa, with PCG-1.5 reaching 2.34 MPa. These values

fall within the range reported for human cancellous bone (2–20 MPa), indicating the scaffolds possess suitable mechanical properties for bone regeneration applications.[49] In summary, the incorporation of an optimal amount of GO (1.0–1.5%) significantly enhances the mechanical performance of PLA/CPP scaffolds, making them promising candidates for use in load-bearing bone tissue engineering. Beyond this threshold, GO agglomeration and reduced crystallinity compromise mechanical integrity.

3.7 The biomineralization activity of PLA/CPP/GO composite scaffolds

The osteoinductive capacity of a scaffold is a critical indicator of its efficacy in bone tissue engineering. To evaluate this, the biomineralization potential of the PLA/CPP/GO composite scaffolds was assessed by examining hydroxyapatite (HA) deposition after immersion in simulated body fluid (SBF) for 3 and 7 days. The corresponding surface morphologies of the samples before SBF immersion (control) are provided in Fig. 1 for comparison.

3.7.1 SEM. As shown in Fig. 7, all scaffolds exhibited notable bio-mineralization activity. After 3 days, granular deposits—confirmed to be hydroxyapatite by complementary XRD and FTIR analyses (Fig. 8)—were observed on the surfaces. By day 7, these deposits had substantially increased, forming a continuous layer, which indicates sustained heterogeneous nucleation and growth of HA. A clear dose-dependent effect of GO content on mineralization efficiency was observed. At GO contents below 1 wt%, the amount of deposited HA did not differ significantly from that of the GO-free control. However, when the GO content exceeded 1.5 wt%, a substantial increase in surface mineralization was evident, with the deposit density rising progressively with GO concentration. This suggests a threshold effect, beyond which GO markedly enhances the biomineralization activity of the scaffold. This enhancement can be attributed to several interrelated factors driven by the incorporation of GO. Firstly, the significantly improved hydrophilicity (as confirmed by contact angle measurements) facilitates better wetting and penetration of SBF into the porous scaffold architecture, thereby promoting ion diffusion and providing a favorable aqueous environment for mineralization.[50] The highly porous structure (porosity > 90%, as reported earlier) offers ample surface area and interfacial contact for ion adsorption and HA nucleation. More importantly, GO nanosheets functionalized with oxygen-containing groups (*e.g.*, carboxyl and hydroxyl) serve as effective nucleation sites for HA. These negatively charged surfaces preferentially attract Ca^{2+} ions from the SBF through electrostatic interactions, leading to local ion enrichment and reducing the energy barrier for HA nucleation.[51] This effect is particularly pronounced at higher GO loadings (>1.5 wt%), where the density of available functional groups is sufficient to overcome the hydrophobic background of PLA. Furthermore, a synergistic effect between GO and CPP is likely at play. As a bioactive component, the presence of CPP provides the necessary chemical environment and calcium-phosphorus ion sources for HA deposition.[52] The high content of GO significantly improves the utilization efficiency of CPP
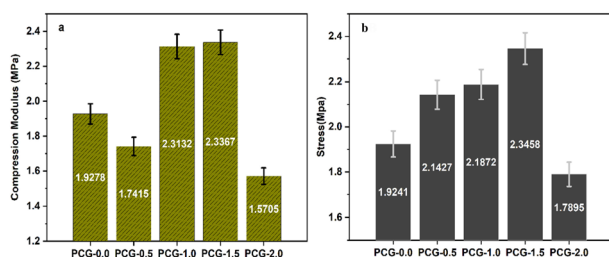
Fig. 6 Compressive modulus (a) and compressive strength (b) of PLA/CPP/GO composite scaffolds with different GO contents.
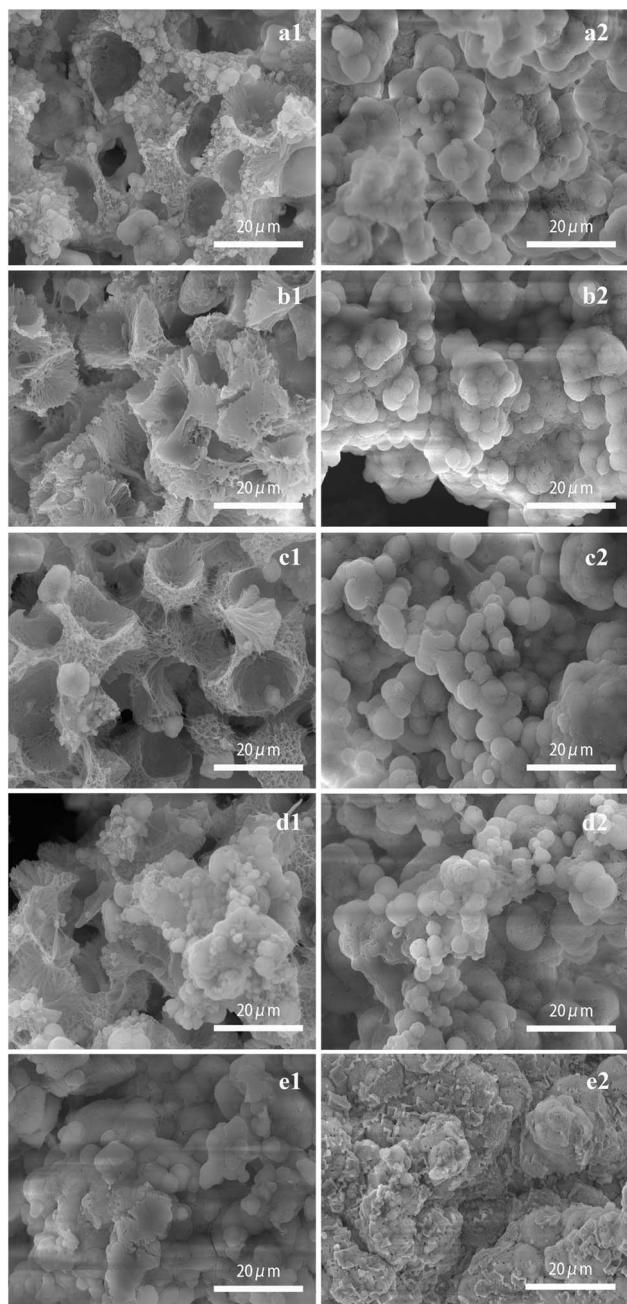
Fig. 7 SEM images of PLA/CPP/GO composites scaffold with different GO contents after immersion in SBF for 3 days and 7 days: (a) PCG-0; (b) PCG-0.5; (c) PCG-1.0; (d) PCG-1.5; (e) PCG-2.0; (a1–e1) is the SEM image after immersion in SBF for 3 days, (a2–e2) is the SEM image after immersion in SBF for 7 days.

Fig. 8 XRD (a) and FTIR (b) graphs of PLA/CPP/GO composite scaffolds with different GO contents after immersion in SBF for 7 days.

degradation products and free ions in SBF on the scaffold surface by optimizing surface hydrophilicity and providing a large number of nucleation sites, thereby synergistically enhancing the mineralization effect. This combination supports a continuous supply of mineral precursors and sufficient nucleation sites, resulting in the observed dense and uniform HA coating after 7 days. In summary, the incorporation of GO above a threshold concentration (1.5 wt%) significantly enhances the biomineralization performance of PLA/CPP
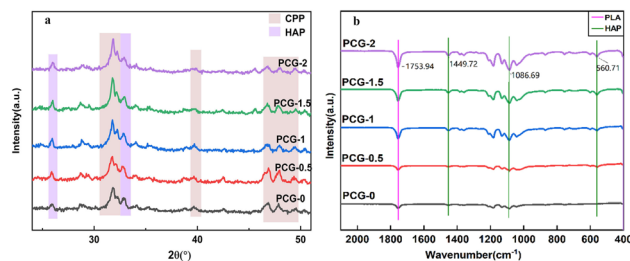
scaffolds by improving hydrophilicity, providing abundant nucleation sites, and synergizing with CPP to promote hydroxyapatite deposition. These findings underscore the potential of GO as a multi-functional bioactive additive in bone tissue engineering scaffolds.

3.7.2 XRD and FTIR. To confirm the composition of the mineralized deposits on the scaffolds, XRD and FTIR analyses were conducted on PLA/CPP/GO composites scaffold after 7 days of immersion in SBF, as presented in Fig. 8. As shown in Fig. 8a, weak diffraction peaks emerged within the range of 31–32°, though the characteristic reflections corresponding to the (211), (112), and (300) crystal planes of hydroxyapatite (HA) were not fully resolved, suggesting the formation of poorly crystalline apatite.[22,53] Notably, with increasing GO content, the intensity of the HA diffraction peak at approximately 26.2° increased consistently and exceeded that of the GO-free composite (Fig. 8a), implying that GO enhances HA crystallization and promotes more effective deposition on the scaffold surface. FTIR spectroscopy further confirmed the formation of carbonated hydroxyapatite (Fig. 8b). Absorption bands observed at 1041 cm^{-1} and 958 cm^{-1} were attributed to the ν_3 and ν_1 vibrational modes of PO_4^{3-}, respectively, while the doublet at 601 cm^{-1} and 561 cm^{-1} corresponds to the ν_4 bending vibrations of PO_4^{3-}. Additionally, peaks at 869 cm^{-1}, 1452 cm^{-1}, and 1438 cm^{-1} are indicative of CO_3^{2-} groups. The presence of carbonate absorption within the 1400–1460 cm^{-1} range confirms the incorporation of carbonate ions into the apatite structure, forming carbonated hydroxyapatite—a composition closely resembling that of biological apatite.[24] In conclusion, the combined XRD and FTIR results confirm that the mineralized layer formed on the scaffolds after SBF immersion consists of poorly crystalline carbonated hydroxyapatite, which demonstrates the excellent bioactivity and apatite-forming ability of the PLA/CPP/GO composites.

3.8 Cytocompatibility of PLA/CPP/GO composite scaffolds

Biocompatibility is a fundamental requirement for bone tissue engineering scaffolds. The cytocompatibility of the PLA/CPP/GO composite scaffolds were evaluated by assessing the proliferation of MC3T3-E1 pre-osteoblasts over 1, 3, and 5 days of culture (Fig. 9). Cell proliferation increased significantly over time on all scaffolds ($P < 0.0001$), confirming general biocompatibility. During the initial culture stage (1–3 days), no statistically significant differences were observed between GO-containing
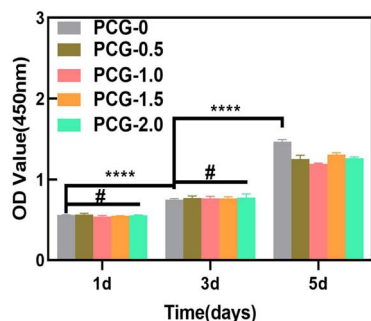
Fig. 9 MC3T3-E1 cell proliferation on PLA/CPP/GO scaffolds after 1, 3, and 5 days of culture ($n = 3$, mean ± SD, $*P < 0.05$, $**P < 0.01$, $***P < 0.001$, $****P < 0.0001$ and $\#P > 0.05$).

scaffolds (0.5–2 wt%) and the pure PLA/CPP control ($P > 0.05$), indicating that GO incorporation did not negatively impact early cell adhesion and survival. This early biocompatibility is likely facilitated by the continuous release of Ca^{2+} and PO_4^{3-} ions from CPP, which activate the calcium-sensing receptor (CaSR) and downstream Wnt/β-catenin signaling pathway, supporting initial cell attachment and cell cycle progression.[54] It has been reported in the literature that the oxygen-containing functional groups on GO can enhance the adsorption of adhesion proteins like fibronectin,[55,56] which may have contributed to the initial cell adhesion observed in our study. By day 5, proliferation on all scaffolds increased markedly compared to earlier time points ($P < 0.0001$). However, all GO-modified scaffolds exhibited significantly lower proliferation rates than the PLA/CPP control ($P < 0.05$), suggesting that higher GO content may inhibit long-term cell expansion. This effect may be attributed to the generation of reactive oxygen species (ROS) induced by GO, leading to oxidative stress and DNA damage.[57] However, the biocompatibility of graphene oxide (GO) remains a subject of debate. Song *et al.* demonstrated that the cytotoxicity of GO is dose-dependent, with low concentrations exerting beneficial effects on cellular activities.[43] Similarly, other studies have indicated that GO does not elicit toxicity within PLA-based composites, but rather promotes cell adhesion and proliferation.[40,58] Notably, the observed reduction in proliferation may coincide with a shift toward osteogenic differentiation. Furthermore, the improved surface hydrophilicity and mineralized microenvironment—as demonstrated in earlier sections—likely support early osteogenic commitment, even in the context of moderated proliferation.[18] In summary, while GO incorporation above 0.5 wt% appears to suppress long-term MC3T3-E1 proliferation, this may indicate a transition from proliferation to differentiation—an advantageous outcome for bone regeneration applications that prioritize functional tissue formation over mere cell numbers.

3.9 Alkaline phosphatase (ALP) activity of PLA/CPP/GO composite scaffolds

The ability of a scaffold to promote osteogenic differentiation is critical for bone regeneration applications. Alkaline phosphatase (ALP), an early marker of osteogenic differentiation, reflects

functional osteoblast activity and is positively correlated with mineralization potential.[59] In this study, ALP activity and staining were used to evaluate the osteoinductive capacity of PLA/CPP/GO scaffolds with varying GO contents (0–2 wt%) after 7 and 14 days of culture with MC3T3-E1 cells. As shown in Fig. 10, ALP activity increased significantly over time across all groups, indicating progressive osteogenic differentiation. However, a clear concentration-dependent effect of GO was observed. After 7 days, the PCG-0.5 group (0.5 wt% GO) exhibited significantly higher ALP activity than both the GO-free control (PCG-0) and groups with higher GO loadings ($P < 0.0001$). The ALP levels in PCG-0 and PCG-1.0 were comparable ($P > 0.05$) but higher than those in PCG-1.5 and PCG-2.0 ($P < 0.05$). This trend persisted at day 14, with PCG-0.5 maintaining superior ALP activity, while the other groups showed no significant differences among themselves ($P > 0.05$). ALP staining results were consistent with these quantitative findings(Fig. 11). The enhanced ALP activity in the PCG-0.5 group suggests that a low concentration of GO optimally promotes osteogenic differentiation. This effect can be attributed to several synergistic factors:[34,56,60,61] (i) the nano-topological cues provided by well-dispersed GO activate YAP/RUNX2 signaling, a key mechanotransduction pathway regulating osteogenesis; (ii) and surface functional groups (*e.g.*, carboxyl) on GO enhance local Ca^{2+} enrichment, synergizing with ions released from CPP to amplify pro-osteogenic calcium signaling.

In contrast, higher GO concentrations (≥1.0 wt%) likely lead to aggregation, which physically hinders nutrient diffusion and cell–matrix interactions, while excessive chelation of calcium ions may disrupt ionic homeostasis and inhibit ALP expression. The sustained increase in ALP activity in PCG-0.5 at 14 days also aligns with the previously observed improvements in hydrophilicity and bio-mineralization, suggesting an integrated microenvironment conducive to osteogenesis. These findings highlight the importance of optimizing GO concentration to balance topological, chemical, and biological cues. The observed discrepancy in the optimal GO content for mechanical reinforcement (1.0–1.5 wt%) *versus* biological activity (0.5 wt%) highlights a key trade-off in composite scaffold design. Higher GO loadings improve stress transfer and stiffness but can lead to aggregation, which reduces the availability of favorable
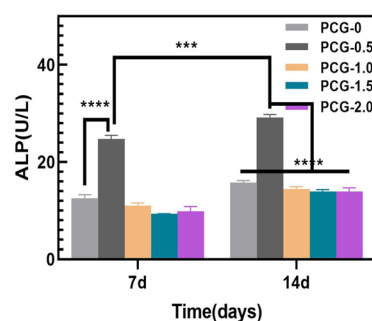

Fig. 10 ALP activity of MC3T3-E1 cells cultured with PLA/CPP/GO composite scaffolds with different GO contents for 7 and 14 days ($n = 3$, mean ± SD, $***P < 0.001$, $****P < 0.0001$).

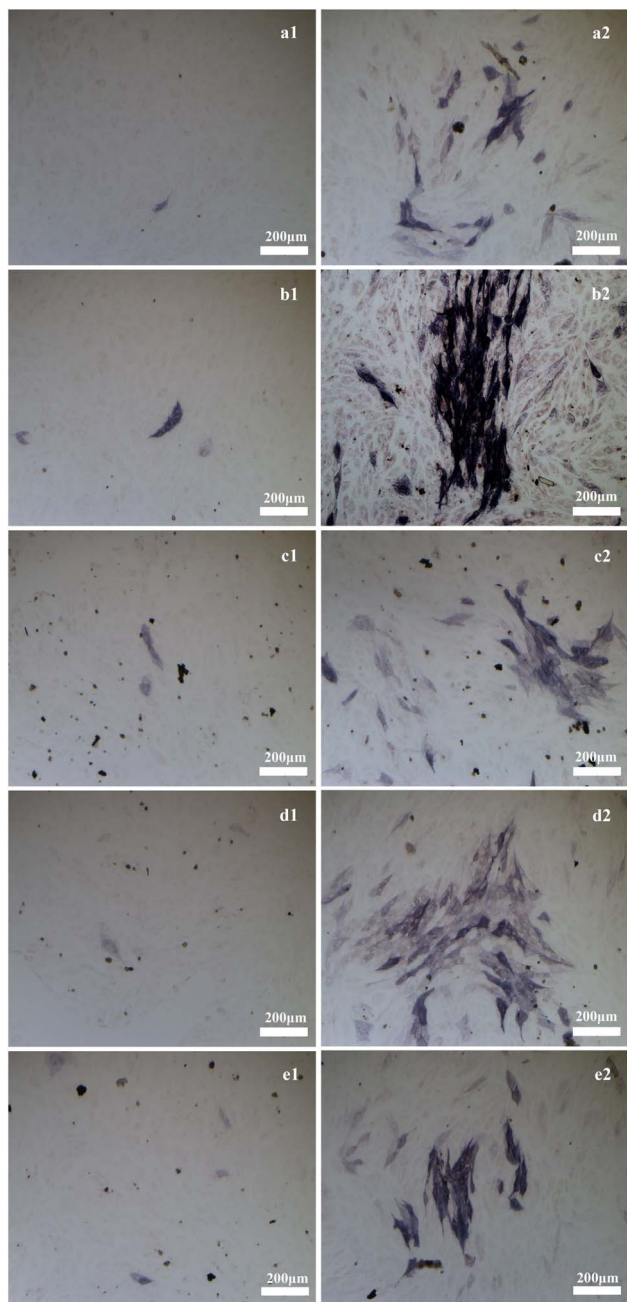© 2025 The Author(s). Published by the Royal Society of Chemistry

Fig. 11 ALP staining of MC3T3-E1 cells cultured with PLA/CPP/GO composite scaffolds with different GO contents for 7 and 14 days, (a) PCG-0; (b) PCG-0.5; (c) PCG-1.0; (d) PCG-1.5; (e) PCG-2.0.

surface sites for cell interaction and may even induce mild cellular stress. Conversely, a lower, well-dispersed GO content (0.5 wt%) provides optimal bioactivity by enhancing hydrophilicity and nucleation sites without the negative effects of aggregation, thereby most effectively promoting the osteogenic differentiation of MC3T3-E1 cells. Future studies could explore surface phosphorylation of GO to further broaden the osteogenic concentration window and enhance biocompatibility. In summary, the incorporation of 0.5 wt% GO significantly enhances the osteoinductive properties of PLA/CPP scaffolds, as

evidenced by elevated ALP activity, demonstrating its potential for bone tissue engineering applications.

3.10 Alizarin Red S staining(ARS) of PLA/CPP/GO composite scaffolds

Alizarin Red S staining was performed to assess the late-stage mineralization potential of MC3T3-E1 cells cultured on PLA/CPP/GO scaffolds with varying GO contents (0%, 0.5%, 1.0%, and 2.0%) for 14 days. As shown in Fig. 12, a distinct enhancement in mineralization was observed specifically in the 0.5% GO group, which exhibited significantly more extensive and intensely stained mineralized nodules compared to all other groups. In contrast, the 0% GO (control), 1.0% GO, and 2.0% GO groups showed comparable levels of mineralization, with no visually prominent differences in the density or extent of calcium deposition among these three compositions. This result highlights a non-monotonic, concentration-specific effect of GO on osteogenic mineralization. The superior performance of the 0.5% GO group aligns consistently with its previously demonstrated peak ALP activity, reinforcing that this specific concentration optimally promotes the osteogenic differentiation of MC3T3-E1 cells. The enhanced mineralization at 0.5% GO can be attributed to the well-dispersed state of GO nanosheets at this low concentration, which provides favorable nano-topographical cues to activate mechanosensitive pathways such as YAP/RUNX2, while its surface functional groups synergize with calcium ions released from CPP to facilitate hydroxyapatite nucleation.[16,50,56,61] Notably, the similar mineralization levels observed among the 0%, 1.0%, and 2.0% GO groups suggest that the beneficial effects of GO are highly dependent on its optimal dispersion. At 1.0% and 2.0% GO, incipient agglomeration may begin to counteract the positive bioactive contributions of well-dispersed GO, without necessarily inducing severe cytotoxicity, thereby resulting in mineralization levels comparable to the GO-free control. This indicates that exceeding the optimal GO loading does not further enhance—but rather neutralizes—the
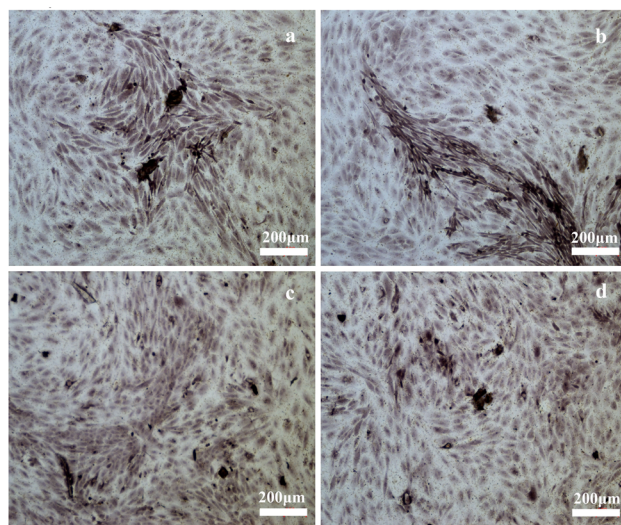

Fig. 12 ARS staining of MC3T3-E1 cells cultured with PLA/CPP/GO composite scaffolds with different GO contents for 14 days, (a) PCG-0; (b) PCG-0.5; (c) PCG-1.0; (d) PCG-2.0.

functional advantage in terms of mineralization output. In conclusion, the Alizarin Red S staining results clearly identify 0.5 wt% as the optimal GO concentration for significantly enhancing the mineralization potential of PLA/CPP-based scaffolds. This specific loading represents a threshold where GO's bioactive benefits are maximized through optimal dispersion and synergistic interaction with CPP, whereas higher concentrations revert the scaffold's mineralization performance to a level similar to GO-free composites.

4. Conclusions

In this study, a series of PLA/CPP/GO composite scaffolds with varying graphene oxide (GO) contents were successfully fabricated *via* phase separation. The incorporation of GO was demonstrated to be an effective strategy for engineering a superior micro-nano architecture that is more biomimetic, hydrophilic, and interconnected. These structural enhancements directly translated to improved biological performance, as detailed below. The incorporation of GO effectively tunes the porosity of PLA/CPP scaffolds without compromising their highly porous nature. The influence of GO content on the scaffold properties exhibited a clear concentration-dependent behavior. An optimal GO loading of 1.0–1.5 wt% significantly enhanced the mechanical performance of the composites, making them promising candidates for load-bearing bone tissue engineering. Beyond this threshold, GO agglomeration and reduced crystallinity compromised the mechanical integrity. Biologically, a distinct optimal concentration was identified. The incorporation of 0.5 wt% GO most effectively promoted the osteoinductive properties, as evidenced by significantly elevated ALP activity. This finding was further corroborated by Alizarin Red S staining, which revealed that the 0.5 wt% GO group yielded the most extensive and dense mineralized nodules after 14 days of culture, outperforming both the control and higher GO content groups (1.0 and 2.0 wt%). The enhanced bioactivity at this optimal concentration is attributed to the synergistic effects of well-dispersed GO nanosheets, which provide nanotopographical cues, and their surface functional groups that synergize with CPP to promote osteogenic differentiation and mineralization. Furthermore, GO incorporation above a threshold concentration (1.0–1.5 wt%) significantly enhanced the biomineralization performance in simulated body fluid by improving hydrophilicity, providing abundant nucleation sites, and synergizing with CPP. The combined XRD and FTIR results confirmed that the mineralized layer formed on the scaffolds consisted of poorly crystalline carbonated hydroxyapatite, demonstrating the excellent bioactivity and apatite-forming ability of the PLA/CPP/GO composites. In summary, this study demonstrates that the properties of PLA/CPP-based scaffolds can be precisely tuned by controlling GO content. Scaffolds containing 0.5–1.0 wt% GO exhibited an optimal balance among mechanical support, porous architecture, biomineralization capacity, and osteogenic potential, making them highly promising for bone repair applications. Future work will focus on surface functionalization of GO to broaden its osteogenic concentration window and

on collaborative *in vivo* studies to validate bone regeneration efficacy, specifically evaluating new bone formation *via* micro-CT, tissue integration through histology, and immune response *via* immunohistochemical analysis.

Conflicts of interest

There are no conflicts to declare.

Data availability

Additional datasets generated and analysed during the current study are available from the corresponding author upon reasonable request.

Acknowledgements

Notes and references

1 W. Wang and K. W. K. Yeung, *Bioact. Mater.*, 2017, **2**, 224–247.

2 D. Cao and J. Ding, *Regen. Biomater.*, 2022, **9**, rbac098.

3 H. Fang, D. Zhu, Q. Yang, Y. Chen, C. Zhang, J. Gao and Y. Gao, *J. Nanobiotechnol.*, 2022, **20**, 26.

4 J. Ma, Y. Li, Y. Mi, Q. Gong, P. Zhang, B. Meng, J. Wang, J. Wang and Y. Fan, *J. Tissue Eng.*, 2024, **15**, 20417314241263689.

5 C. De Soricellis, C. Amante, P. Russo, R. P. Aquino and P. Del Gaudio, *Pharmaceutics*, 2025, **17**, 129.

6 X. Mo, D. Zhang, K. Liu, X. Zhao, X. Li and W. Wang, *Int. J. Mol. Sci.*, 2023, **24**, 1291.

7 Z. Liu, M. Tilieke, Y. Zhou, M. Ming, H. Zhang, L. Chen, R. Zheng, Y. Jie, X. Shu, J. Guan, S. Ling, X. Chen and Z. Shao, *J. Mater. Chem. B*, 2025, **13**, 10331–10342.

8 H. Xie, Z. Gu, C. Li, C. Franco, J. Wang, L. Li, N. Meredith, Q. Ye and C. Wan, *Ceram. Int.*, 2016, **42**, 2386–2392.

9 P. A. Comeau, H. Frei, C. Yang, G. Fernlund and F. M. Rossi, *J. Biomater. Appl.*, 2012, **27**, 267–275.

10 M. Neufurth, X. Wang, S. Wang, R. Steffen, M. Ackermann, N. D. Haep, H. C. Schröder and W. E. G. Müller, *Acta Biomater.*, 2017, **64**, 377–388.

11 Q. Dong, L. C. Chow, T. Wang, S. A. Frukhtbeyn, F. Wang, M. Yang and J. W. Mitchell, *Colloids Surf., A*, 2014, **457**, 256–262.

12 M. Šupová, *Materials*, 2020, **13**, 327.

13 S. Li, Z. Niu, Y. Jiao, P. Jin, D. Yang, C. Bai, J. Liu, G. Li and Y. Luo, *RSC Adv.*, 2022, **12**, 22806–22814.

14 S. H. M. Wong, S. S. Lim, T. J. Tiong, P. L. Show, H. F. M. Zaid and H. S. Loh, *Int. J. Mol. Sci.*, 2020, **21**, 5202.

15 G. Shen, H. Ren, Q. Shang, W. Zhao, Z. Zhang, X. Yu, K. Tang, J. Tang, Z. Yang, D. Liang and X. Jiang, *EBioMedicine*, 2020, **52**, 102626.

16 X. Yang, Q. Zhao, J. Chen, J. Liu, J. Lin, J. Lu, W. Li, D. Yu and W. Zhao, *Stem Cell. Int.*, 2021, **2021**, 1–12.

17 D. Xu, C. Wang, J. Wu, Y. Fu, S. Li, W. Hou, L. Lin, P. Li, D. Yu and W. Zhao, *ACS Omega*, 2022, **7**, 13546–13556.

18 J. H. Ahn, I.-R. Kim, Y. Kim, D.-H. Kim, S.-B. Park, B.-S. Park, M.-K. Bae and Y.-I. Kim, *Nanomaterials*, 2020, **10**, 620.

19 A. M. Díez-Pascual and A. L. Díez-Vicente, *ACS Appl. Mater. Interfaces*, 2016, **8**, 17902–17914.

20 C. Liang, Y. Luo, G. Yang, D. Xia, L. Liu, X. Zhang and H. Wang, *Nanoscale Res. Lett.*, 2018, **13**, 15.

21 R. Zeinali, L. J. Del Valle, J. Torras and J. Puiggalí, *Int. J. Mol. Sci.*, 2021, **22**, 3504.

22 S. Liu, Y. Zheng, Z. Wu, J. Hu and R. Liu, *Polymer*, 2020, **211**, 123093.

23 S. Liu, Y. Zheng, R. Liu and C. Chao, *J. Mater. Sci.: Mater. Med.*, 2020, **31**, 1–11.

24 S. Liu, Z. He, G. Xu and X. Xiao, *Mater. Sci. Eng. C*, 2014, **44**, 201–208.

25 X. Liu and P. X. Ma, *Biomaterials*, 2009, **30**, 4094–4103.

26 T. Xu, Q. Yao, J. M. Miszuk, H. J. Sanyour, Z. Hong, H. Sun and H. Fong, *Colloids Surf., B*, 2018, **171**, 31–39.

27 S. Lopez De Armentia, J. C. Del Real, E. Paz and N. Dunne, *Materials*, 2020, **13**, 5083.

28 E.-S. Motiee, S. Karbasi, E. Bidram and M. Sheikholeslam, *Int. J. Biol. Macromol.*, 2023, **247**, 125593.

29 B. Illing, L. Mohammadnejad, A. Theurer, J. Schultheiss, E. Kimmerle-Mueller, F. Rupp and S. Krajewski, *Materials*, 2023, **16**, 7307.

30 K. Qiao, L. Xu, J. Tang, Q. Wang, K. S. Lim, G. Hooper, T. B. F. Woodfield, G. Liu, K. Tian, W. Zhang and X. Cui, *J. Nanobiotechnol.*, 2022, **20**, 141.

31 Y. Wang, Y. Zhao, L. Qiao, F. Zou, Y. Xie, Y. Zheng, Y. Chao, Y. Yang, W. He and S. Yang, *Bioact. Mater.*, 2021, **6**, 2089–2104.

32 F. Roshanfar, S. Hesaraki and A. Dolatshahi-Pirouz, *Biology*, 2022, **11**, 751.

33 S. Liu, W. Li, Z. Xu, J. Hu, F. Wu and Y. Zheng, *Polymers*, 2022, **14**, 5348.

34 C. Wu, Y. Tang, B. Mao, X. Yan, Y. Pu and K. Zhao, *Colloids Surf., B*, 2021, **205**, 111898.

35 S.-S. Park, Y.-S. Lee, S.-W. Lee, E. Repo, T.-H. Kim, Y. Park and Y. Hwang, *Polymers*, 2023, **15**, 269.

36 T. Zhou, J. Zhou, S. Zhang and S. Cui, *Adv. Healthcare Mater.*, 2025, **14**, 2501332.

37 Z. Fan, J. Wang, Z. Wang, H. Ran, Y. Li, L. Niu, P. Gong, B. Liu and S. Yang, *Carbon*, 2014, **66**, 407–416.

38 B. Oktay, E. Ahlatcıoğlu Özerol, A. Sahin, O. Gunduz and C. B. Ustundag, *ChemistrySelect*, 2022, **7**, e202200697.

39 X. Cheng, T. Li, L. Yan, Y. Jiao, Y. Zhang, K. Wang, Z. Cheng, J. Ma and L. Shao, *Sci. Adv.*, 2023, **9**, eadh8195.

40 C. Zhang, L. Wang, T. Zhai, X. Wang, Y. Dan and L.-S. Turng, *J. Mech. Behav. Biomed. Mater.*, 2016, **53**, 403–413.

41 S. Yang, P. Lei, Y. Shan and D. Zhang, *Appl. Surf. Sci.*, 2018, **435**, 832–840.

42 J. Lu, C. Sun, K. Yang, K. Wang, Y. Jiang, R. Tusiime, Y. Yang, F. Fan, Z. Sun, Y. Liu, H. Zhang, K. Han and M. Yu, *Polymers*, 2019, **11**, 1009.

43 J. Song, H. Gao, G. Zhu, X. Cao, X. Shi and Y. Wang, *Carbon*, 2015, **95**, 1039–1050.

44 K. R. Remya, S. Chandran, S. Mani, A. John and P. Ramesh, *J. Biomater. Sci., Polym. Ed.*, 2018, **29**, 1444–1462.

45 X. Wang, G. Song and T. Lou, *J. Mater. Sci.: Mater. Med.*, 2010, **21**, 183–188.

46 M. Ruoß, V. Häussling, F. Schügner, L. H. H. Olde Damink, S. M. L. Lee, L. Ge, S. Ehnert and A. K. Nussler, *Bioengineering*, 2018, **5**, 86.

47 S. Braccini, C. Tacchini, F. Chiellini and D. Puppi, *Int. J. Mol. Sci.*, 2022, **23**, 3265.

48 A. Seyedsalehi, L. Daneshmandi, M. Barajaa, J. Riordan and C. T. Laurencin, *Sci. Rep.*, 2020, **10**, 22210.

49 B. Coppola, L. Montanaro and P. Palmero, *J. Funct. Biomater.*, 2022, **13**, 148.

50 Z. E. Dibazar, L. Nie, M. Azizi, H. Nekounam, M. Hamidi, A. Shavandi, Z. Izadi and C. Delattre, *Materials*, 2023, **16**, 2799.

51 L. Angelova, A. Daskalova, R. Mincheva, E. Filipov, A. Dikovska, M. H. Fernandes, S. Vig and I. Buchvarov, *Opt. Quant. Electron.*, 2024, **56**, 1195.

52 P. N. De Aza, A. H. De Aza, P. Pena and S. De Aza, *Bol. Soc. Espanola Ceram. Vidr.*, 2007, **46**(2), 45.

53 C. Yao, J. Zhu, A. Xie, Y. Shen, H. Li, B. Zheng and Y. Wei, *Mater. Sci. Eng. C*, 2017, **73**, 709–715.

54 J. Wang, Q. Zhao, L. Fu, S. Zheng, C. Wang, L. Han, Z. Gong, Z. Wang, H. Tang and Y. Zhang, *Bioact. Mater.*, 2022, **15**, 446–455.

55 C. Wang, S. Gao, R. Lu, X. Wang and S. Chen, *Cells*, 2022, **11**, 3417.

56 A. Srion, F. Thammarakcharoen, W. Chokevivat, W. Suvannapruk and J. Suwanprateep, *Int. J. Mol. Sci.*, 2025, **26**, 5633.

57 D. Mohammadrezaei, H. Golzar, M. Rezai Rad, M. Omidi, H. Rashedi, F. Yazdian, A. Khojasteh and L. Tayebi, *J. Biomed. Mater. Res.*, 2018, **106**, 2284–2343.

58 Q. Zhang, Q. Tu, M. E. Hickey, J. Xiao, B. Gao, C. Tian, P. Heng, Y. Jiao, T. Peng and J. Wang, *Colloids Surf., B*, 2018, **172**, 496–505.

59 M. S. Saveleva, A. N. Ivanov, J. A. Chibrikova, A. A. Abalymov, M. A. Surmeneva, R. A. Surmenev, B. V. Parakhonskiy, M. V. Lomova, A. G. Skirtach and I. A. Norkin, *Macromol. Biosci.*, 2021, **21**, 2100266.

60 S. Zheng, L. Xu, L. Bo, E. Gao, E. Zheng, L. Xie, B. Zhao, J. Yi, Y. Li, Y. Xu, Y. Wang and B. Tao, *Mater. Today Bio*, 2025, 101831.

61 Y. Luo, H. Shen, Y. Fang, Y. Cao, J. Huang, M. Zhang, J. Dai, X. Shi and Z. Zhang, *ACS Appl. Mater. Interfaces*, 2015, **7**, 6331–6339.